AIChE

Power-Law Polymer Solution Flow in a Converging Annular Spinneret: Analytical Approximation and Numerical Computation

Kuo-Lun Tung, Yu-Ling Li, Che-Chia Hu, and Yu-Shao Chen
R&D Center for Membrane Technology, Dept. of Chemical Engineering, Chung Yuan University, Chung-Li 320, Taiwan

DOI 10.1002/aic.12561
Published online March 22, 2011 in Wiley Online Library (wileyonlinelibrary.com).

A simplified analytical solution for the flow of power-law liquids through a conical annulus was derived to estimate the flow profile, wall shear rate, and elongation rate in the spinneret during the spinning of hollow fiber membranes. The velocity profiles and shear and elongation rates of the power-law fluid showed good agreement with those obtained from computational fluid dynamic simulations. Although the actual spinneret is characterized by an annulus with a converging cross section, most studies to date have used a geometrical concentric annulus for the sake of simplicity. The results of the current work indicate that neglecting the converging characteristics of the actual spinneret can lead to significant underestimation of the wall shear rate. Using the equations derived in our work, we were able to predict not only the velocity profile but also the wall shear rate and the elongation rate; the influence of the spinneret design on the membrane morphology and properties were also examined. © 2011 American Institute of Chemical Engineers *AIChE J,* 58: 122–131, 2012
Keywords: power-law fluid, converging annulus, conical spinneret, hollow fiber membrane, shear rate

Introduction

Because of the simplicity and low cost, membrane techniques have been used in a wide range of applications to separate gaseous and liquid mixtures. Two different configurations of membranes are generally used: flat plate membranes and hollow fiber membranes. Although these two types of membranes show equal performance for separation purposes, hollow fiber membranes possess more advantageous characteristics, such as (1) a higher membrane packing density than flat membranes and (2) the ability to be self-supported and back flushable.[1]

The parameters controlling the spinning of hollow fibers are quite complicated and very different from those used to prepare flat plate membranes. In the case of hollow fiber spinning, membrane researchers have focused on various aspects to obtain hollow fiber membranes exhibiting excellent separation performance. These aspects include the composition of the dope solution, the composition of the bore liquid and external coagulant, quench conditions, the air gap length, bore fluid flow rate, humidity, and fiber take-up speed.[2–18] When the polymer dope is pumped through the spinneret during hollow fiber spinning, the highest shear stress is located at the wall of the spinneret. Thus, the rheological conditions existing in the spinneret during hollow fiber spinning are essential to control the final membrane morphology and properties. Many researchers have studied the effects of the dope extrusion rate on dry-jet wet spun hollow fibers. Aptel et al.[13] found that increasing the dope

Additional Supporting Information may be found in the online version of this article.

Correspondence concerning this article should be addressed to K.-L. Tung at kuolun@cycu.edu.tw.

extrusion rate could reduce the permeability. Chung et al.[14–16] have also investigated the effect of the shear stress and shear rate within the spinneret on the morphology and properties of the hollow fiber membranes. Their results revealed that the fibers had a lower permeability due to the greater molecular orientation but a higher selectivity with increasing shear rates. They also found that when the dope extrusion rate exceeded a critical value, the performance was no longer significantly affected.[17,18] This observation has also been confirmed by using infrared reflection spectroscopy.[19–21] However, a quantitative analysis is needed to systematically study the effects of the flow conditions during spinning on the final morphology and properties of the hollow fiber membranes.

Shilton[22] was the first to present a methodology to establish the flow profile in the spinneret during the spinning of hollow fiber membranes. The flow equations were derived for a power-law fluid passing through a concentric annulus spinneret. To characterize the effects of shear stress in the spinneret, Qin and Chung[17] worked with a spinneret with a high aspect ratio of the die length and flow channel gap to calculate the shear rate at the outer wall of the concentric annulus during hollow fiber membrane spinning. This particularly high aspect ratio was used to neglect the end effects in the tapered exit for the theoretical analysis. However, for the sake of simplicity, the most widely theoretically studied geometry is generally a concentric annulus, although the actual spinneret is characterized by an annulus with a converging cross section. Wang et al.[23] further extended the analysis of straight annular spinnerets to conical ones, and they experimentally showed that the response of the macrovoids was different for various flow angles in the spinnerets. They concluded that the flow angle in the spinneret was another variable controlling the morphology of the hollow fiber membranes.

To date, due to the complexity of non-Newtonian hydrodynamics in a converging cross-section annulus, the analytical study of polymeric fluid flows in a conical spinneret with a converging cross-section is still elusive. Computational fluid dynamic (CFD) methods have been widely used in the membrane module design.[24–29] Cao et al.[24] were the first to use CFD methods to simulate the flow profile of a doped solution in a spinneret having three different flow angles. The shear and elongation rates at the spinneret outlet were analyzed. On the basis of simulation results, they proposed a hypothetical mechanism for the change of polymer conformation at large elongation and shear rates. The degree of polymer alignment was increased with increasing shear rate and the presence of elongational kinematics in the flow direction led to further extension of the polymer chains. Although CFD simulations can be used to calculate the shear and elongation rates in the spinneret to understand the polymer chain alignment behavior, an analytical method seems to be more convenient for engineers to be applied to predict the flow behavior in a hollow fiber spinneret as well as the design of a new spinneret.

In this study, a simplified analytical method to predict the flow behavior of a power-law fluid through an annulus spinneret with a converging cross section is proposed. This method allows us to estimate the flow and wall shear-rate profiles in the spinneret during the spinning of hollow fiber membranes. Using the derived equation, we could predict not only the velocity profile, but also the shear and elongation rates; the effect of the spinneret design on the membrane morphology and properties could also be examined. The calculated velocity profiles and the shear and elongation rates in the spinneret were also compared for a power-law fluid with CFD simulation predictions as well as with CFD results from the literature.

Theoretical Study

In this theoretical study, both an analytical method and CFD simulations were used to analyze the hydrodynamics in the conical annulus spinneret during the spinning of hollow fiber membranes. The following assumptions were made in the theoretical derivation and in the simulations: (1) laminar flow, (2) steady state, (3) no-slip boundary conditions at the wall, (4) power-law fluid, and (5) isothermal. An additional assumption was used for the theoretical derivation: that of a fully developed flow for any cross section along the flow direction.

Analytical derivation

A schematic diagram of the converging annulus spinneret is shown in Figure 1a. To facilitate the mathematical treatment, the annulus was divided into three sections, including a converging section between the first and the third sections; the corresponding geometrical variables are defined as follows.

Geometrical Variables. We introduce the following dimensionless variables in an axisymmetric cylindrical coordinate system:

$$(r,z) \rightarrow (\xi,\zeta) : \xi = \frac{r}{R} \quad \text{and} \quad \zeta = \frac{z}{R}. \tag{1}$$

The slope ε of the converging section can be defined using the dimensionless variables, (ξ, ζ), as follows:

$$\xi = 1 - \varepsilon\zeta. \tag{2}$$

The inner radii of the annulus for Section I and Section III in Figure 1a are R and αR, respectively, and the length of the converging section is βR. The relationship between the geometrical variables α, β, and ε can be expressed by:

$$\varepsilon = \frac{1-\alpha}{\beta}. \tag{3}$$

The inner radius for Section II in Figure 1a is δR, so the geometrical variable δ can be expressed as:

$$\delta = 1 - \varepsilon\zeta. \tag{4}$$

It should be noted that the variable δ is a function of ζ, i.e., a function of z.

Momentum Balance. To facilitate the mathematical treatment of the momentum balance, the annulus was divided into three sections, with a converging middle section in Figure 1a. In the limit of very slow, it is reasonable to adjust the maximum velocity such that the amount of fluid flowing through each cross section is constant.

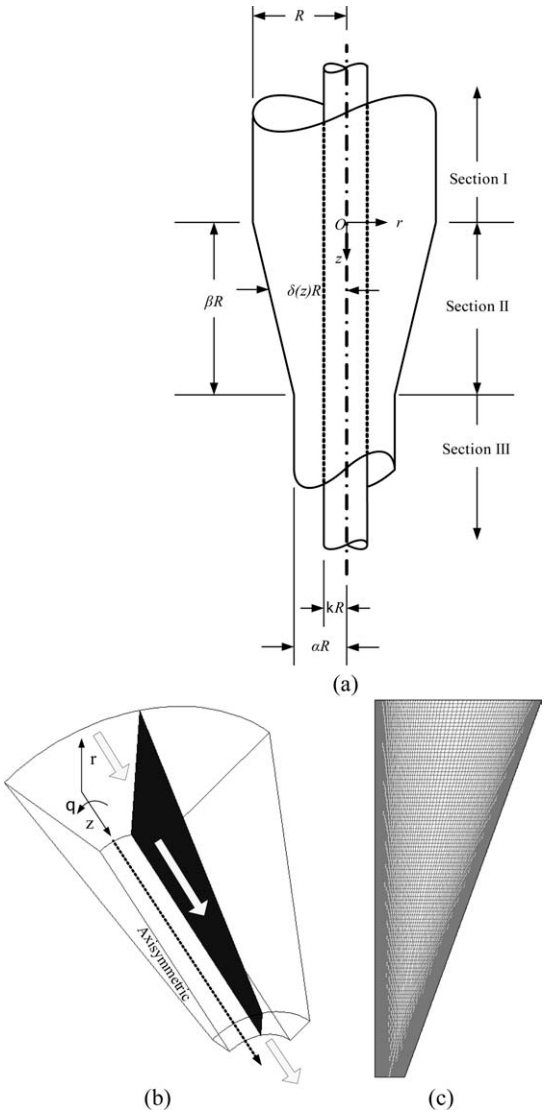

Figure 1. Schematic diagram of the conical annulus spinneret: (a) ideal system, (b) simulation system, and (c) mesh type.

Section I. When a fluid is pumped through an annulus, the z-component of the momentum balance equation may be written in cylindrical coordinates in terms of a shear rate[30]:

$$0 = -\frac{1}{r}\frac{d}{dr}(r\tau_{rz}) - \frac{dP}{dz}. \tag{5}$$

If the maximum velocity occurs at $r = \lambda R$, Eq. 5 can be integrated to give

$$\tau_{rz} = \frac{\Delta P}{2L}\left(r - \frac{(\lambda R)^2}{r}\right). \tag{6}$$

The variable λ is an underdetermined constant in Section I of Figure 1a and scales with ζ, i.e., z, in Section II of Figure 1a. The stress rate of deformation relationship of the polymer solutions for spinning is assumed to be of the generalized power-law form, i.e.,[31]

$$\tau = -m\left|\frac{\mathbf{D}:\mathbf{D}}{2}\right|^{(n-1)/2}\mathbf{D}, \tag{7}$$

where $\mathbf{D}$ is the rate of deformation tensor. For a simple shear flow, the generalized power-law model for the spinning of polymer solutions can be simplified as follows:

$$\tau_{rz} = -m\left|\frac{dV_z}{dr}\right|^{n-1}\left(\frac{dV_z}{dr}\right). \tag{8}$$

Because dV_z/dr is negative in tube flow, the Eq. 8 can be further rearranged as a power-law model:

$$\tau_{rz} = m\left(-\frac{dV_z}{dr}\right)^n. \tag{9}$$

The velocity profile of the spinning flow can be solved by substituting Eq. 9 into Eq. 6 and using the boundary condition $V_z = 0$ at $r = \kappa R$ and $r = R$, which leads to:

$$V_{z,I} = R\left(\frac{\Delta PR}{2mL}\right)^s \int_{\kappa}^{\xi}\left(\frac{\lambda^2}{\xi} - \xi\right)^s d\xi \quad \text{for} \quad \kappa \le \xi \le \lambda, \quad \text{and} \tag{10a}$$

$$V_{z,I} = R\left(\frac{\Delta PR}{2mL}\right)^s \int_{\xi}^{1}\left(\xi - \frac{\lambda^2}{\xi}\right)^s d\xi \quad \text{for} \quad \lambda \le \xi \le 1, \tag{10b}$$

where $s = 1/n$. The parameter λ can be determined by numerically solving the following equation:

$$\int_{\kappa}^{\lambda}\left(\frac{\lambda^2}{\xi} - \xi\right)^s d\xi = \int_{\lambda}^{1}\left(\xi - \frac{\lambda^2}{\xi}\right)^s d\xi. \tag{11}$$

The volumetric flow rate of the power-law fluid in an annulus can be calculated according to:

$$\begin{aligned} Q_I &= \int_{\kappa R}^{R} 2\pi r V_z dr = \int_{\kappa R}^{\lambda R} 2\pi r V_z dr + \int_{\lambda R}^{R} 2\pi r V_z dr \\ &= 2\pi R^3\left(\frac{\Delta PR}{2mL}\right)^s\left[\int_{\kappa}^{\lambda}\int_{\kappa}^{\xi}\left(\frac{\lambda^2}{\rho} - \rho\right)^s d\rho\xi d\xi\right] \\ &\quad + 2\pi R^3\left(\frac{\Delta PR}{2mL}\right)^s\left[\int_{\lambda}^{1}\int_{\xi}^{1}\left(\rho - \frac{\lambda^2}{\rho}\right)^s d\rho\xi d\xi\right] \\ &= \pi R^3\left(\frac{\Delta PR}{2mL}\right)^s \int_{\kappa}^{1}\left|\lambda^2 - \xi^2\right|^{s+1}\xi^{-s}d\xi. \end{aligned} \tag{12}$$

The shear rate at the outer wall in Section I of Figure 1a is:

$$\begin{aligned} \left|\frac{dV_z}{dr}\right|_{r=R} &= \left(\frac{\Delta PR}{2mL}\right)^s\left[1 - \lambda^2\right]^s \\ &= \frac{Q}{\pi R^3}\frac{\left(1 - \lambda^2\right)^s}{\int_{\kappa}^{1}\left|\lambda^2 - \xi^2\right|^{s+1}\xi^{-s}d\xi}. \end{aligned} \tag{13}$$

This equation was derived by Frederickson and Bird.[32] Shilton[22] was the first to apply this methodology to estimate the shear rate induced in a spinneret during the spinning of hollow fiber membranes by assuming that the spinneret was an annulus with a constant cross-sectional radius.

Section II. Because the amount of fluid flowing through each cross section is a constant,

$$Q_{\mathrm{I}} = Q_{\mathrm{II}}. \tag{14}$$

The velocity profile can then be modified as follows:

$$V_{z,\mathrm{II}} = R\left(\frac{\Delta PR}{2mL}\right)^s \int_{\kappa}^{\xi} \left(\frac{\lambda^2}{\xi} - \xi\right)^s d\xi \quad \text{for} \quad \kappa \le \xi \le \lambda, \quad \text{and} \tag{15a}$$

$$V_{z,\mathrm{II}} = R\left(\frac{\Delta PR}{2mL}\right)^s \int_{\xi}^{\delta(\zeta)} \left(\xi - \frac{\lambda^2}{\xi}\right)^s d\xi \quad \text{for} \quad \lambda \le \xi \le \delta(\zeta). \tag{15b}$$

The parameter λ can be determined by numerically solving the following equation:

$$\int_{\kappa}^{\lambda} \left(\frac{\lambda^2}{\xi} - \xi\right)^s d\xi = \int_{\lambda}^{\delta(\zeta)} \left(\xi - \frac{\lambda^2}{\xi}\right)^s d\xi. \tag{16}$$

The volumetric flow rate can be expressed as:

$$\begin{aligned} Q_{\mathrm{II}} &= \int_{\kappa R}^{\delta R} 2\pi r V_z dr = \int_{\kappa R}^{\lambda R} 2\pi r V_z dr + \int_{\lambda R}^{\delta R} 2\pi r V_z dr \\ &= 2\pi R^3 \left(\frac{\Delta PR}{2mL}\right)^s \left[\int_{\kappa}^{\lambda}\int_{\kappa}^{\xi} \left(\frac{\lambda^2}{\rho} - \rho\right)^s d\rho\xi d\xi\right] \\ &+ 2\pi R^3 \left(\frac{\Delta PR}{2mL}\right)^s \left[\int_{\lambda}^{\delta}\int_{\xi}^{\delta} \left(\rho - \frac{\lambda^2}{\rho}\right)^s d\rho\xi d\xi\right] \\ &= \pi R^3 \left(\frac{\Delta PR}{2mL}\right)^s \int_{\kappa}^{\delta} \left|\lambda^2 - \xi^2\right|^{s+1} \xi^{-s} d\xi. \end{aligned} \tag{17}$$

The local shear rate at the outer wall in Section II of Figure 1a is thus:

$$\begin{aligned} \dot{\gamma}|_{r=\delta(z)R} &= \left|\frac{dV_z}{dr}\right|_{r=\delta(z)R} = \left(\frac{\Delta PR}{2mL}\right)^s \left[\delta - \frac{\lambda^2}{\delta}\right]^s \\ &= \frac{Q}{\pi R^3} \frac{\left(\delta - \frac{\lambda^2}{\delta}\right)^s}{\int_{\kappa}^{\delta} \left|\lambda^2 - \xi^2\right|^{s+1} \xi^{-s} d\xi}. \end{aligned} \tag{18}$$

The local shear rate at the inner wall in Section II of Figure 1a is:

$$\begin{aligned} \dot{\gamma}|_{r=\kappa R} &= \left|\frac{dV_z}{dr}\right|_{r=\kappa R} = \left(\frac{\Delta PR}{2mL}\right)^s \left[\kappa - \frac{\lambda^2}{\kappa}\right]^s \\ &= \frac{Q}{\pi R^3} \frac{\left(\kappa - \frac{\lambda^2}{\kappa}\right)^s}{\int_{\kappa}^{\delta} \left|\lambda^2 - \xi^2\right|^{s+1} \xi^{-s} d\xi}. \end{aligned} \tag{19}$$

This equation can be used to estimate the local shear rate induced in a spinneret with a converging cross section during the spinning of hollow fiber membranes. Details of MATLAB programs for modeling calculation are given as a Supporting Information.

CFD simulations

Simulation System. To understand the transport phenomena for various spinneret structures, a commercially available CFD software package (FLUENT) was used to calculate the flow field. The simulation system and computational cells (10,000) for a converging annulus spinneret are illustrated in Figures 1b, c. In this two-dimensional (z-r plane) axisymmetric simulation study of the flow profile in a converging annulus spinneret, the wall effects in the θ-direction were neglected. Therefore, the assumption of zero velocity in the θ-direction is explicitly stated in this work. Figure 2 shows a three-dimensional view of the meshes used to approximate a real hollow fiber spinneret. To examine the validity of the analytical estimation method, the analytical results were compared not only with the simulation data for the ideal conical spinneret shown in Figure 1 but also with those obtained for a real hollow fiber spinneret (Figure 3).

Governing Equations for Fluid Flow. The flow field was obtained by solving the continuity equation and the momentum-balance equations of the system. The flow of fluid in the domain of this study was assumed to be steady state and isothermal. In addition, the spinneret structure was assumed to have the no-slip boundary condition. The governing equations for steady-state fluid flow in the converging annulus spinneret are the equation of continuity and the equations of motion. The continuity and momentum equations for the two-dimensional axisymmetric simulation system are as follows[33]:

Continuity Equation

$$\frac{\partial}{\partial r}(\rho V_r) + \frac{\partial}{\partial z}(\rho V_z) + \frac{\rho V_r}{r} = 0; \tag{20}$$

Momentum Equation

$$\begin{aligned} &\frac{1}{r}\frac{\partial}{\partial z}(r\rho V_z V_z) + \frac{1}{r}\frac{\partial}{\partial r}(r\rho V_r V_z) \\ &\quad = -\frac{\partial P}{\partial z} + \frac{1}{r}\frac{\partial}{\partial z}\left[r\mu\left(2\frac{\partial V_z}{\partial z} - \frac{2}{3}\left(\frac{\partial V_z}{\partial z} + \frac{\partial V_r}{\partial r} + \frac{V_r}{r}\right)\right)\right] \\ &\qquad + \frac{1}{r}\frac{\partial}{\partial r}\left[r\mu\left(\frac{\partial V_z}{\partial r} + \frac{\partial V_r}{\partial z}\right)\right], \end{aligned} \tag{21a}$$

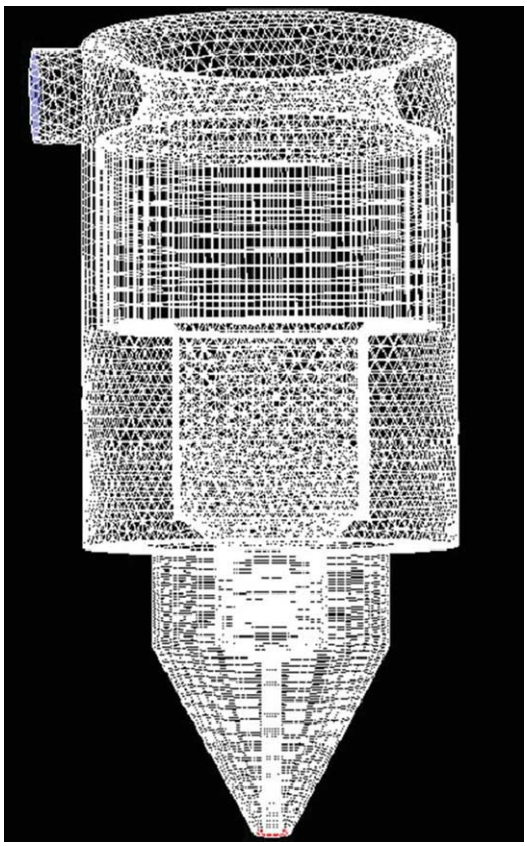

Figure 2. Schematic diagram of the 3-D calculation grid of the conical annulus spinneret used in the numerical simulation.

[Color figure can be viewed in the online issue, which is available at wileyonlinelibrary.com.]

$$\frac{1}{r}\frac{\partial}{\partial z}(r\rho V_z V_r)+\frac{1}{r}\frac{\partial}{\partial r}(r\rho V_r V_r) = -\frac{\partial P}{\partial r}+\frac{1}{r}\frac{\partial}{\partial z}\left[r\mu\left(\frac{\partial V_r}{\partial z}+\frac{\partial V_z}{\partial r}\right)\right] +\frac{1}{r}\frac{\partial}{\partial r}\left[r\mu\left(2\frac{\partial V_r}{\partial r}-\frac{2}{3}\left(\frac{\partial V_z}{\partial z}+\frac{\partial V_r}{\partial r}+\frac{V_r}{r}\right)\right)\right] -2\mu\frac{V_r}{r^2}+\frac{2}{3}\frac{\mu}{r}\left(\frac{\partial V_z}{\partial z}+\frac{\partial V_r}{\partial r}+\frac{V_r}{r}\right)+\frac{\rho V_z^2}{r}, \quad (21b)$$

where μ is apparent viscosity of non-Newtonian-power-law fluid. It can be expressed as

$$\mu = m\left(-\frac{\partial V_z}{\partial r}\right)^{n-1}, \quad (22)$$

where m is a measure of the average viscosity of the fluid (the consistency index); n is a measure of the deviation of the fluid from non-Newtonian (the power-law index). The boundary conditions for Eqs. 20 and 21 are:

Velocity Inlet

$$V_z = V, \quad V_r = 0, \quad (23)$$

Walls of Converging Annulus Spinneret

$$V_z = V_r = 0. \quad (24)$$

The differential equations of interest, such as the general conservation of mass and momentum, were integrated over each control volume, assuming a power-law functional form for the variations of the dependent variables between adjacent nodes to evaluate the integrals.

The semi-implicitly method for pressure-linked equations-consistent algorithm with a power-law difference scheme and a single direction sweep solution method were used in this study. This method basically involves dividing the calculation domain into a number of nonoverlapping control volumes, each containing a cell node at its center. The result for each control volume is an algebraic equation containing unknown values of the dependent variables for the central grid and its immediate neighbors. The algebraic equations corresponding to all control volumes in the calculation domain are then iteratively solved to obtain discrete values for the dependent variables. The sum of the normalized residuals for all variables converges to less than 1×10^{-4} within 7000–8000 iterations.

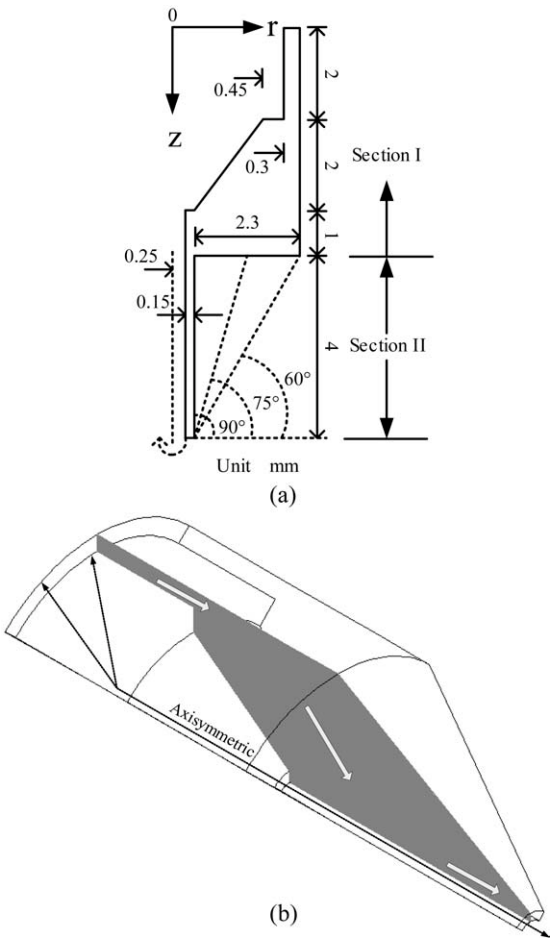

Figure 3. Schematic diagram of the conical annulus spinneret: (a) three real systems and (b) a simulation system.

Table 1. Dimensions of the Conical Annulus Spinnerets

Variables	Values
R (mm)	1.983
αR (mm)	0.600
βR (mm)	3.800
κR (mm)	0.300

Results and Discussion

In this study, the analytical solutions for both straight and ideal conical spinnerets (Table 1) were compared with CFD simulations. For the real conical spinneret, the effect of various flow angles on the shear rate, elongation rate, and velocity profile is thoroughly discussed in the following sections, which also compare the analytical and CFD simulation results.

Validity of the analytical solutions

A theoretical study is a convenient way to estimate the effect of the spinneret geometry on the shear rate, elongation rate, and velocity profile for a power-law fluid flowing through a spinneret. In addition, it constitutes a useful tool to improve the spinneret design. In this study, we first chose to investigate the flow in a straight spinneret, even though this model has already been well studied in the literature. The shear-rate distribution in a straight spinneret can be calculated by considering the rheological data n; the geometrical dimensions of the spinneret, R, αR, βR, and κR; and the flow rate of the dope fluid, Q, in the theoretical analysis. Furthermore, numerical calculations were performed using commercial software (MATLAB). Figure 4 shows the radial shear-rate distribution in a straight spinneret for various values of n for the dope fluid. Values for ξ of 0.5 and 1 represent the locations at the inner and outer walls, respectively. The result show that the analytical solutions agreed well with CFD simulation results because the fully developed assumption in the analytical solution was a good approximation of the flow in a straight annulus. In addition, we observed that the shear-rate distributions were different for different values of n. These differences are mainly due to the fact that a shear-thinning fluid (i.e., $n = 0.8$) tends to flow more easily under a high shear stress than a shear-thickening fluid. Considering the flow in the straight spinneret, the shear stress is higher at the wall and approaches zero near the center of the flow channel. As a result, for a shear-thinning fluid, the shear rate is higher near the wall and lower near the center of the flow channel. This increase in the shear rate near the wall is critical because it can force the polymer chains to align with the flow direction, which can lead to a decrease in the permeability and increase in the selectivity of the resulting hollow fiber membrane.

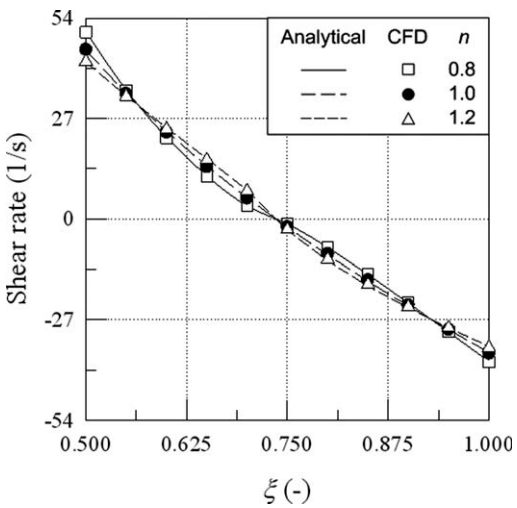

Figure 4. Comparison between the analytical solution and CFD simulations for the shear-rate distribution in the exit of the straight spinneret for various n values (Q = 0.1 mL/min).

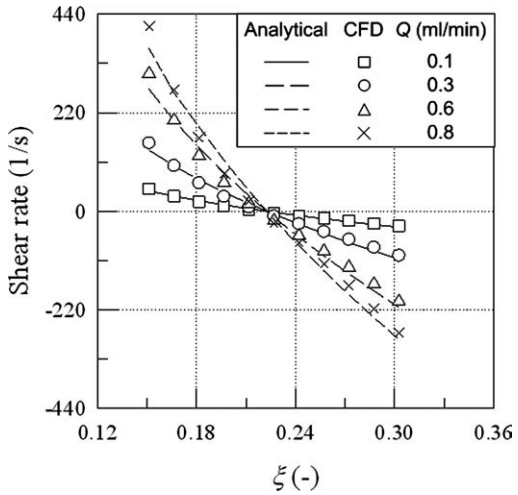

Figure 5. Comparison between the analytical solution and CFD simulations for the shear-rate distribution in the converging spinneret exit for various dope fluid flow rates (n = 1).

The effect of the flow rate on the radial shear-rate distribution in a converging spinneret is illustrated in Figure 5. The results show that the analytical results and the CFD simulation data agree with each other when the liquid flow rate is low. However, a deviation of about 12% can be observed in the region near the walls at high flow rates. The analytical solution underestimated the shear stress at the inner wall and overestimated that at the outer wall. The discrepancy between these two methods can be attributed to the fact that the velocity in the r-direction is neglected in the analytical calculation. The velocity in r direction is vanished for a one-dimensional flow in a straight spinneret, but the effect of the velocity in r direction would become more pronounced in a converging spinneret. In addition, as the flow rate of the dope fluid was increased, we also observed that the shear rate increased because of the higher fluid velocity.

Figure 6 shows the shear-rate distribution in the axial direction at the inner and outer walls of a converging spinneret. The parameter ζ denotes the distance from the entrance of the spinneret. In this figure, we show that the analytical solution underestimates the shear rate of the fluid at the inner wall and overestimates that at the outer wall, compared with the CFD simulations; the discrepancy between

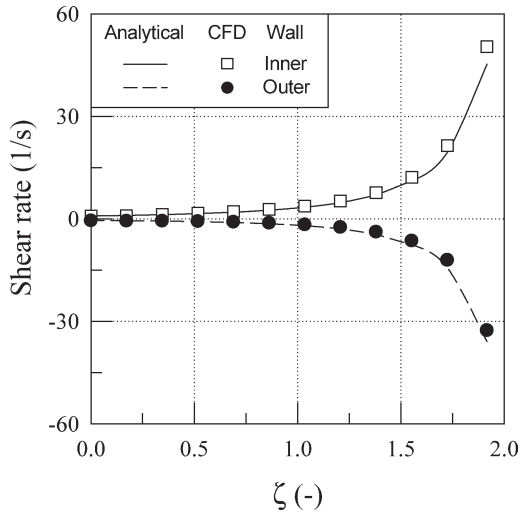

Figure 6. Comparison between the analytical solution and CFD simulations for the shear-rate distribution at the inner and outer walls of the converging spinneret ($n = 1$, $Q = 0.1$ mL/min).

these two methods increases along the direction of flow. At the entrance of the spinneret, the boundary conditions are the same for the two methods and consequently, no deviations are observed. However, these deviations become more apparent along the z-axis because we have neglected the velocity in the r-direction in the analytical solution. In addition, both the analytical and CFD simulation results show that the absolute values of the shear rate increase along the axial direction before reaching a maximum at the exit of the spinneret. This is due to the decrease of the annular surface area in the converging spinneret along the direction of flow, which results in a higher fluid flow rate.

Effect of various flow angles on the shear rate for real conical spinnerets

To confirm the validity of the theoretical analysis, the analytical solutions were compared with the work by Cao et al.[24] and Shilton.[22] The geometry of the real conical spinneret used in the study of Cao et al.[24] is shown in Figure 3. The rheological properties of the dope solution can be described using the power-law expression:

$$\tau = 129.66\,\dot{\gamma}^{1.423}\,. \tag{25}$$

Figure 7 shows a comparison between the analytical solutions and the CFD simulations for the shear-rate distribution in a real conical spinneret for a flow angle of 90°. The analytical and simulation predictions are in good agreement with the calculations by Cao et al.[24] and Shilton.[22] In addition, we observe that the shear rates calculated using the method of Cao et al.[24] are in good agreement with those predicted by Shilton.[22] In the study of Cao et al.,[24] the results showed that the simulation predictions disagreed with the data of Shilton[22] for $n = 0.7026$, which is the inverse of 1.423. Therefore, we believe that there may be some errors in the simulation parameters reported by Cao et al.[24]

The shear-rate distribution along the z-axis at the inner and outer walls of real conical spinnerets was also investigated for various flow angles using an analytical method and CFD simulations. The results are shown in Figures 8a, b. A dimensionless distance along the z-direction was used instead of ζ, due to the different values of R obtained when the angle of the spinneret was varied. A discrepancy was observed between the analytical solution and the CFD simulations at the entrance of the spinneret because of the different boundary conditions used in these two calculations. The actual flow profile of the dope fluid at the entrance of the real conical spinneret is quite complex, whereas the analytical solution simply assumes that the fluid has already achieved its fully developed profile at this location. The difference between these two methods was observed to vanish along the z-axis when the spinneret angle was 90°. However, for angles of 60° and 75°, the velocity in the r-direction had to be considered because of the varying annulus surface area, leading to a disagreement between the two predictions. The absolute value of the shear rate was found to be underestimated at the inner wall and overestimated at the outer wall by the analytical solution, which was confirmed by the results obtained for the converging spinneret.

The difference of the position of the maximum velocity along the z-axis in Section II of Figure 1a of the spinneret between the simplified analytical solution and the CFD simulation has also been illustrated in Figure 9. This discrepancy is caused by the neglect of the velocity in the r-direction. Although, the velocity in the r-direction had to be considered because of the varying annulus surface area, the maximum errors of the shear rate (dV_z/dr) at the outer wall obtained between the simplified analytical solution and the CFD simulation are only 0.56%, 4.39%, and 13.61% for angles of 90°, 75°, and 60°, respectively, as shown in Figure 8a; the maximum errors of the shear rate (dV_z/dr) at the inner wall are only 0.90%, 0.81%, and 12.82% for angles of 90°, 75°, and 60°, respectively, as shown in Figure 8b. These estimations proved that the proposed simplified analytical

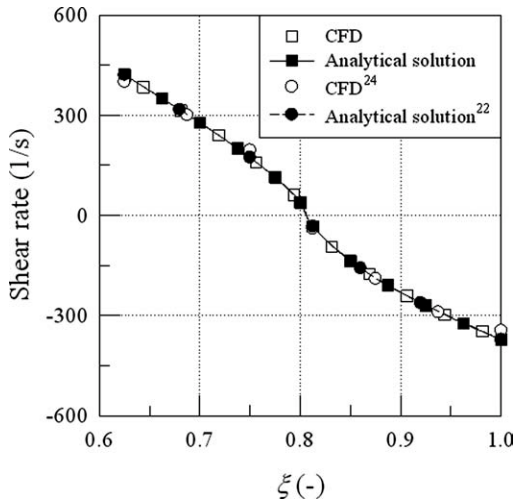

Figure 7. Comparison between the analytical solution and CFD simulations for the shear-rate distribution in a real conical spinneret for a flow angle of 90° ($n = 1.423$, $Q = 0.2$ mL/min).

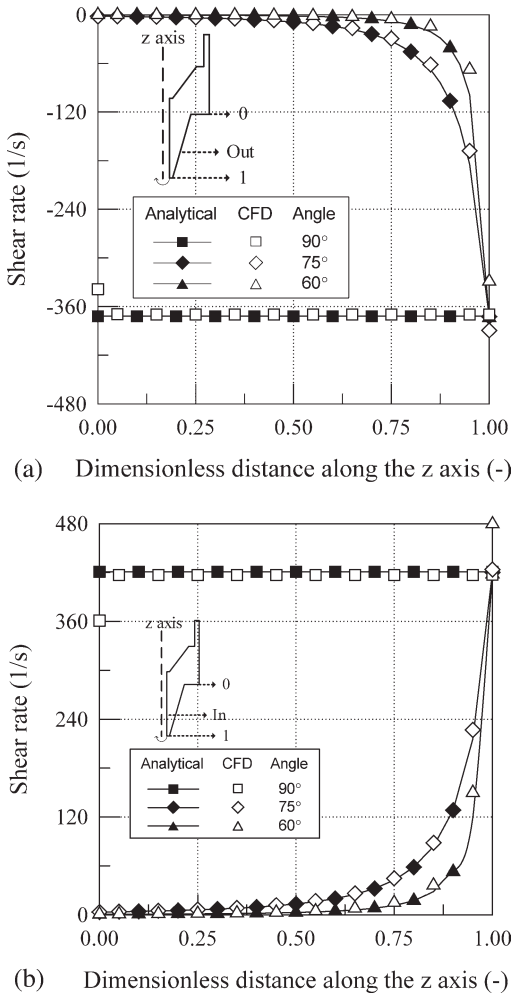

Figure 8. Effect of various flowing angles on the shear-rate distribution in a real conical spinneret: (a) outer wall and (b) inner wall (n = 1.423, Q = 0.2 mL/min).

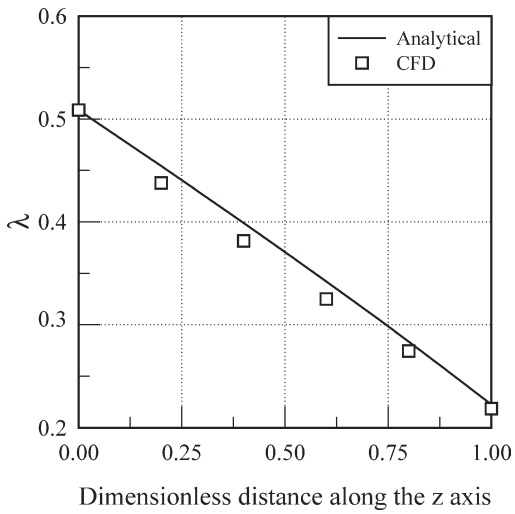

Figure 9. Difference of the position of the maximum velocity along the z-axis in Section II of Figure 1a of the spinneret between the simplified analytical solution and the CFD simulation.

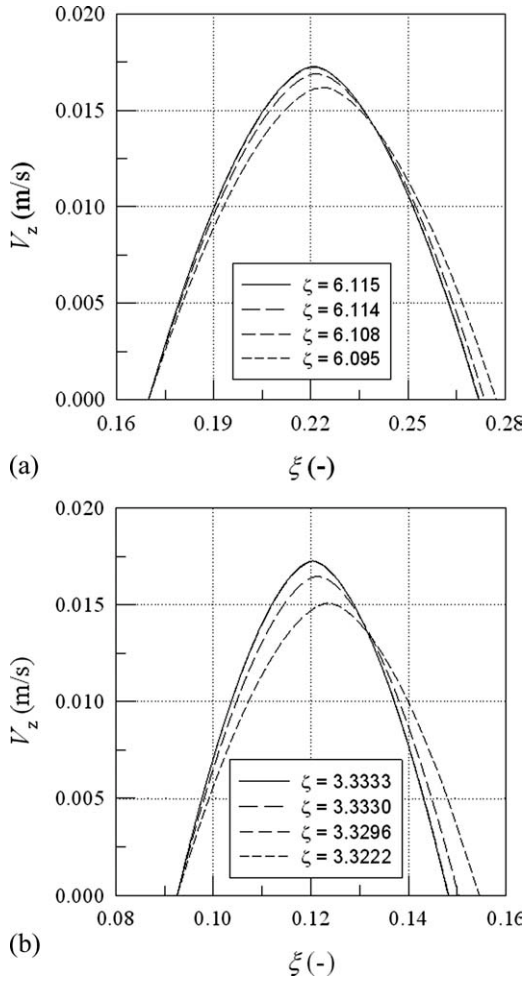

Figure 10. Effect of various positions along the z-axis on the z-velocity distribution in a real conical spinneret for flow angles of: (a) 75° and (b) 60° (n = 1.423, Q = 0.2 mL/min).

solution is a good approximation for predicting the fluid flow behavior in the converging annual spinneret.

Effect of various flow angles on the elongation rate of real conical spinnerets

A straight spinneret lacks elongation flow because the velocity profile is constant along the z-direction. As a result, the elongation rate has rarely been investigated using computational models because most past studies have focused on straight spinnerets. In this study, the elongation rate distribution in a conical spinneret was calculated for different flow angles using both an analytical method and CFD simulations. The elongation rate is defined as:

$$\text{Elongation rate} = \frac{\partial V_z}{\partial z}. \tag{26}$$

Evaluation of the elongation rate involves calculating the axial velocity profile at different axial positions. It should be noted that because a steady-state assumption was adopted in this theoretical modeling derivation, the Lagrangian unsteadiness, especially evident for the time-dependent viscoelastic

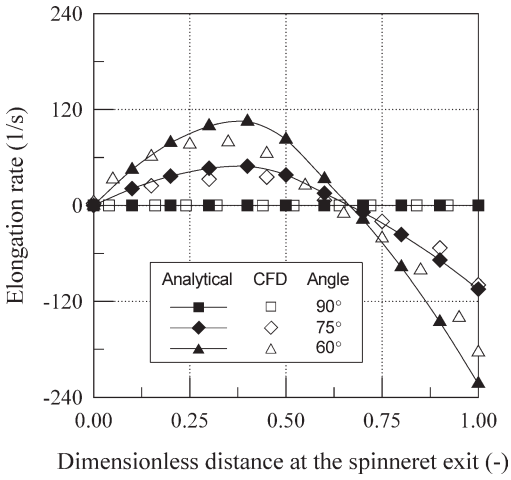

Figure 11. Effect of various flow angles on the elongation rate at the exit of a real conical spinneret (n = 1.423, Q = 0.2 mL/min).

fluid, is not taken into consideration in this study. Figures 10a, b show the axial velocity distribution of a conical spinneret in the r-direction at four different axial positions for the two flow angles 75° and 60°, respectively. Note that the four ζ values in Figure 10a correspond to the same axial positions as in Figure 10b; any discrepancy in the two values is due to the difference in R values for the two flow angles. The axial velocity increases with increasing radial distance and reaches a maximum value. The position of the maximum velocity depends on the ratio of the radii of the inner and outer walls, and therefore varies along the axial direction. In addition, the value of the maximum velocity increases with increasing ζ because the annular area in a conical spinneret becomes smaller along the axial direction. When comparing Figures 10a, b, it is expected that the velocity for a given axial position decrease with decreasing flow angle because of the larger annular area at smaller flow angles.

Figure 11 shows the effect of various flow angles in real conical spinnerets on the elongation rate distribution at the exit of the spinnerets. We observe that the elongation rate vanishes when the flow angle equals 90° because the axial velocity is constant along the direction of flow. In addition, the absolute value of the elongation rate at the outer wall clearly increases when the spinneret flow angle is reduced. Cao et al.[24] reported that an increase in the elongation rate of the dope fluid led to a stretching of the polymer chains and an enhancement of chain packing in the outer skin of hollow fiber membranes, resulting in better membrane selectivity and reduced membrane permeance for gas separation applications. In other words, the selectivity and the permeance of a hollow fiber membrane can be controlled by the flow angle of the spinneret. In Figure 11, we also show that the analytical results are roughly equivalent to those obtained from CFD simulations for flow angles of 90° and 75°. However, the discrepancy becomes much more pronounced for an angle of 60°, and the analytical solution overestimates the elongation rate. The discrepancy between these two methods is mainly attributed to the fact that the velocity in the r-direction is unknown for the analytical solution.

Conclusions

In this study, the effect of various flow angles on the shear and elongation rates was investigated using an analytical approach and CFD simulations. An analytical solution for a power-law fluid flowing through a converging annulus was derived to investigate the flow and the wall shear-rate profiles in a spinneret during the spinning of hollow fiber membranes. The results show that the analytical solution tends to overestimate the shear stress at the outer wall and to underestimate that at the inner wall for a converging spinneret. In case of a real conical spinneret, there is a discrepancy at the entrance of the spinneret because different boundary conditions were used for the analytical and CFD methods. However, in most of the flow regions, the analytical solution was in good agreement with the CFD simulation results, and the derived equation could conveniently predict the pressure drop, velocity profile, shear rate, and elongation rate during spinning. As a result, this theoretical technique constitutes a useful methodology to optimize the membrane morphology and properties. As future work, we will use plane-polarized infrared spectroscopy to measure the molecular orientation in the active layer of hollow fiber membranes and check the validity of the current results.

Acknowledgments

The authors thank the Ministry of Economic Affairs (MOEA), R.O.C., for the grant for the Technology Development Program for Academia (TDPA) project; the Center-of-Excellence (COE) Program on Membrane Technology from the Ministry of Education (MOE), R.O.C.; and the National Science and Technology Program—Energy, National Science Council (NSC), R.O.C. for their financial support.

Notation

D = the rate of deformation tensor, 1/s
L = annulus length, m
m = power-law model consistency, Pa.s^n
n = power-law index, dimensionless
P = Pressure, Pa
Q = flow rate of the dope fluid, L/s
Q_i = flow rate of the dope fluid for section i, with $i \in$ (I, II, III), L/s
r = radial coordinate, m
R = outer radius of the annulus of Section I in Figure 1a, m
s = power-law constant, dimensionless
t = time, s
T = Temperature, K
V = velocity of fluid at the inlet, m/s
V_i = velocity of fluid along the i-coordinate direction, with $i \in (r, z)$, m/s
z = axial coordinate, m

Greek letters

α = ratio of the inner radius of the outer tube of Section III in Figure 1a to the radius of Section I in Figure 1a in a conical annulus
β = ratio of the converging section length to the inner radius of theannulus in Section I of Figure 1a
$\dot{\gamma}$ = shear rate, 1/s
θ = angular coordinate
δ = ratio of the outer radius of Section II to that of Section I in a conical annulus in Figure 1a
ε = slope of the converging section in a conical annulus
ζ = dimensionless axial coordinate
κ = ratio of the outer radius of the inner pipe to the inner radius of the outer pipe in Section I of Figure 1a in a conical annulus
λ = dimensionless radial position at which the shear stress vanishes
μ = apparent viscosity of non-Newtonian-power-law fluid, Pa s
ξ = dimensionless radial coordinate
ρ = density, kg/m^3
τ = shear stress, N/m^2

Literature Cited

1. Mulder M. *Basic Principle of Membrane Technology*, 2nd ed. Dordrecht, The Netherlands: Kluwer Academic, 1996.
2. Cabasso I, Klein E, Smith JK. Polysulfone hollow fiber. II. Morphology. *J Appl Polym Sci*. 1977;21:165–180.
3. Chung TS, Kafchinski ER, Vora R. Development of a defect-free 6FDA-durene asymmetric hollow fiber and its composite hollow fibers. *J Membr Sci*. 1994;88:21–36.
4. Wang D, Li K, Teo WK. Polyethersulfone hollow fiber gas separation membranes prepared from NMP/alcohol solvent systems. *J Membr Sci*. 1996;115:85–108.
5. Xu ZL, Chung TS, Huang Y. Effect of polyvinylpyrrolidone molecular weights on morphology, oil/water separation, mechanical and thermal properties of polyetherimide/polyvinylpyrrolidone hollow fiber membranes. *J Appl Polym Sci*. 1999;74:2220–2233.
6. Ismail AF, Lau WJ. Theoretical studies on structural and electrical properties of PES/SPEEK blend nanofiltration membrane. *AIChE J*. 2009;55:2081–2093.
7. Bonyadi S, Chung TS, Rajagopalan R. A novel approach to fabricate macrovoid-free and highly permeable PVDF hollow fiber membranes for membrane distillation. *AIChE J*. 2009;55:828–833.
8. Wang KY, Chung TS. Polybenzimidazole nanofiltration hollow fiber for cephalexin separation. *AIChE J*. 2006;52:1363–1377.
9. Chung TS, Teoh SK, Hu X. Formation of ultrathin high-performance polyethersulfone hollow fiber membrane. *J Membr Sci*. 1998;133: 161–175.
10. Van't Hof JA, Reuvers AJ, Boom RM, Rolevink HHM, Smolders CA. Preparation of asymmetric gas separation membranes with high selectivity by a dual-bath coagulation method. *J Membr Sci*. 1992;70: 17–30.
11. Miao X, Sourirajan S, Zhang H, Lau WWY. Production of polyethersulfone hollow fiber ultrafiltration membrane, part I. Effects of water (internal coagulant) flow rate and length of air gap. *Sep Sci Technol*. 1996;31:141–172.
12. Ekiner OM, Vassilatos G. Polyaramide hollow fibers for H_2/CH_4 separation. II. Spinning and properties. *J Membr Sci*. 2001;186: 71–84.
13. Aptel P, Abidine N, Ivaldi F, Lafaille JP. Polysulfone hollow fibers-effect of spinning conditions on ultrafiltration properties. *J Membr Sci*. 1985;22:199–215.
14. Chung TS, Teoh SK, Lau WWY, Srinivasan MP. Effect of shear stress within the spinneret on hollow fiber membrane morphology and separation performance. *Ind Eng Chem Res*. 1998;37:3930–3938; Correction: *Ind Eng Chem Res*. 1998;37:4903.
15. Chung TS, Lin WH, Vora RH. The effect of shear rate on gas separation performance of 6FDA-durene polyimide hollow fiber. *J Membr Sci*. 2000;167:55–66.
16. Qin JJ, Wang R, Chung TS. Investigation of shear stress effect within a spinneret on flux, separation and thermomechanical properties of hollow fiber ultrafiltration membranes. *J Membr Sci*. 2000; 175:197–213.
17. Qin JJ, Chung TS. Effect of dope flow rate on morphology, separation performance, thermal and mechanical properties of ultrafiltration hollow fiber membranes. *J Membr Sci*. 1999;157:35–51.
18. Chung TS, Qin JJ, Gu J. Effect of shear rate within the spinneret on morphology, separation performance and mechanical properties of ultrafiltration polyethersulfone hollow fiber membrane. *Chem Eng Sci*. 2000;55:1077–1091.
19. Xue G, Jiang S, Dai C, Zhu W, Seng R. Characterization of orientation at polyester fiber surface by modified infrared reflection technique. *Polym Bull*. 1986;15:363–368.
20. Ismail AF, Shilton SJ, Dunkin IR, Gallivan SL. Direct measurement of rheologically induced molecular orientation in gas separation hollow fibre membranes and effects on selectivity. *J Membr Sci*. 1997;126:133–137.
21. Idris A, Ismail AF, Noorhayati M, Shilton SJ. Measurement of rheologically induced molecular orientation using attenuated total reflection infrared dichroism in reverse osmosis hollow fiber cellulose acetate membranes and influence on separation performance. *J Membr Sci*. 2003;213:45–54.
22. Shilton SJ. Flow profile induced in spinneret during hollow fiber membrane spinning. *J Appl Polym Sci*. 1997;65:1359–1362.
23. Wang KY, Takeshi M, Chung TS, Guo WF. The effects of flow angle and shear rate within the spinneret on the separation performance of poly(ether sulfone) (PES) ultrafiltration hollow fiber membranes. *J Membr Sci*. 2004;240:67–79.
24. Cao C, Chung TS, Chen SB, Dong ZJ. The study of elongation and shear rates in spinning process and its effect on gas separation performance of poly(ethersulfone) (PES) hollow fiber membranes. *Chem Eng Sci*. 2004;59:1053–1062.
25. Li YL, Tung KL. CFD simulation of fluid flow through spacer-filled membrane module: selecting suitable cell types for periodic boundary conditions."*Desalination*. 2008;233:351–358.
26. Li YL, Tung KL. The effect of curvature of spacer-filled channel on fluid flow in spiral-wound membrane modules. *J Membr Sci*. 2009; 319:286–297.
27. Li YL, Tung KL, Lu MY, Huang SH. Mitigating the curvature effect of the spacer-filled channel in a spiral-wound membrane module. *J Membr Sci*. 2009;329:106–118.
28. Duran JE, Mohseni M, Taghipour F. Computational fluid dynamics modeling of immobilized photocatalytic reactors for water treatment. *AIChE J*. DOI: 10.1002/aic.12399.
29. Kim AS, Lee YT. Laminar flow with injection through a long dead-end cylindrical porous tube: application to a hollow fiber membrane. *AIChE J*. DOI: 10.1002/aic.12430.
30. Bird RB, Armstrong RC, Hassager O. *Dynamics of Polymeric Liquids. Vol. 1: Fluid Mechanics*, 2nd ed. New York: Wiley, 1987.
31. Jarzebeski AB, Wilkinson WL. Non-isothermal developing flow of a generalized power-law fluid in a tapered tube. *J Non-Newtonian Fluid Mech*. 1981;8:239–248.
32. Frederickson AG, Bird RB. Non-Newtonian flow in annuli. *Ind Eng Chem*. 1958;50:347–352.
33. FLUENT, Inc. *FLUENT V 6.2.16 Users Manual*. Lebanon, NH: FLUENT, Inc, 2005.

Manuscript received Mar. 1, 2010, and revision received Dec. 16, 2010.